Towards Optical Optimization of Planar Monolithic Perovskite/Silicon-Heterojunction Tandem Solar Cells

Steve Albrecht[1], Michael Saliba[2], Juan-Pablo Correa-Baena[3], Klaus Jäger[4], Lars Korte[1], Anders Hagfeldt[3], Michael Grätzel[2], and Bernd Rech[1]

[1] *Insitute for Silicon Photovoltaics and* [4]*Young Investigator Group Nano-SIPPE: Nanostructured Silicon for Photonic and Photovoltaic Implementations Helmholtz-Zentrum Berlin für Materialien und Energie GmbH, Institut für Silizium-Photovoltaik, Kekuléstraße 5, 12489 Berlin, Germany.*

[2] *Laboratory of Photonics and* [3]*Laboratory of Photomolecular Science Swiss Federal Institute of Technology (EPFL), Station 6, Lausanne, CH 1015, Switzerland.*

ABSTRACT

Combining inorganic-organic perovskites and crystalline silicon into a monolithic tandem solar cell has recently attracted increased attention due to the high efficiency potential of this cell architecture. Promising results with published efficiencies above 21% have been reported so far. To further increase the device performance, optical optimizations enabling device related guidelines are highly necessary. Here we experimentally show the optical influence of the ITO thickness in the interconnecting layer and fabricate an efficient monolithic tandem cell with a reduced ITO layer thickness that shows slightly improved absorption within the silicon sub-cell and a stabilized power output of 17%. Furthermore we present detailed optical simulations on experimentally relevant planar tandem stacks to give practical guidelines to reach efficiencies above 25%. By optimizing the thickness of all functional and the perovskite absorber layers, together with the optimization of the perovskite band-gap, we present a tandem stack that can yield ca. 17.5 mA/cm² current in both sub-cells at a perovskite band-gap of 1.73 eV including losses from reflection and parasitic absorption. Assuming that the higher band-gap of the perovskite absorber directly translates into a higher open circuit voltage, the perovskite sub-cell should be able to reach a value of 1.3 V. With that, realistic efficiencies above 28% are within reach for planar monolithic tandem cells in which the thickness of the perovskite top-cell and the perovskite band-gap is highly optimized. When applying light trapping schemes such as textured surfaces and by reducing the parasitic absorption of the functional layer, for example in spiro-OMeTAD, this monolithic tandem can overcome 30% power conversion efficiency.

TOC / GRAPHICAL ABSTRACT

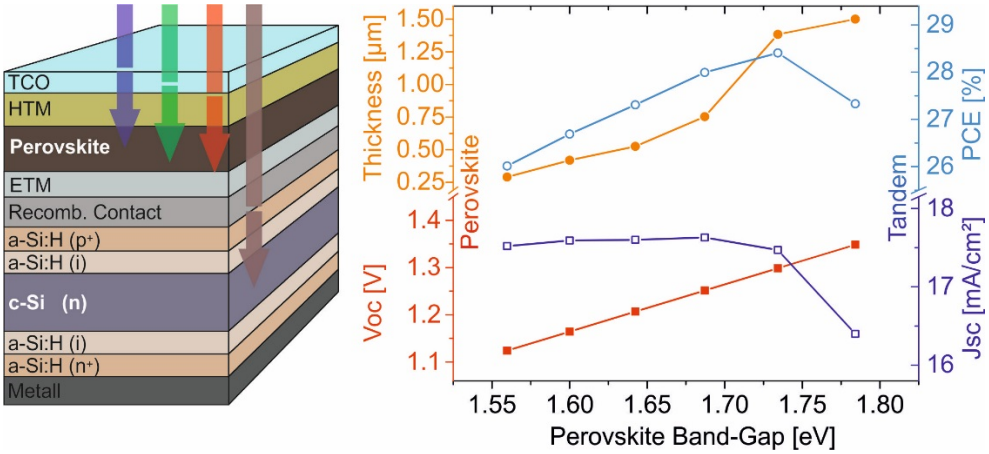

KEY WORDS

perovskite solar cells, silicon heterojunction, monolithic tandem solar cell, optical simulation, semitransparent solar cell

INTRODUCTION

Accompanied by the discovery of their superior optoelectronic properties, an outstanding rise in power conversion efficiency during the last six years was shown for solar cells based on organic-inorganic perovskite materials such as $CH_3NH_3PbI_3$.[1] Today, certified power conversion efficiencies reach over 21%[1,2] and values as high as 21.1% have been reported[3,4] for cells based on this class of materials. Due to the high optical band-gap of ca. 1.56 eV that is close to the optimum when combining with crystalline silicon (c-Si), the market leading PV technology, perovskite materials are promising absorbers for high-efficiency perovskite/silicon tandem applications.[5-7]

In the perovskite/silicon tandem cell, the wide gap perovskite cell is stacked on top of a silicon bottom cell. High energy photons are then absorbed within the perovskite top-cell and converted to charge carriers at a high voltage. Low energy photons are absorbed by the c-Si bottom cell. Thus, a wide spectral range of absorption is covered by the tandem, in order to gain a high photocurrent. As a consequence, the radiative losses from thermalization of high energy photons well above the silicon optical band-gap are reduced, since these photons are captured by the perovskite top-cell. These radiative losses account for more than 50%[8] of the overall losses in silicon single junctions and get reduced to around 35% for perovskite/silicon tandem cells. Thus, in theory, efficiency limits of 30-35%[5,9,10] have been calculated based on optical and electrical simulations of perovskite/silicon tandem architectures. This is well above state-of-the-art silicon single junction efficiencies, for which a "practical limit" of ~26% has been estimated.[11,12] Current champion cells, which are based on amorphous/crystalline silicon heterojunctions similar to those used in the present study (albeit with both contacts on the cell's rear side) are very close to this practical limit with record efficiencies of 25.6%.[13]

In principle, there are two distinct basic tandem cell architectures: 4-terminal and 2-terminal (monolithic) devices. When building a 4-terminal device, two solar cells are processed

individually and then mechanically stacked on top of each other. This enables more flexibility during processing. So far efficiencies between 13 and 22.8% have been reported for this cell architecture.[6,14-17] In monolithic devices all layers are processed directly on top of each other. Thus, the layer processing of the perovskite top cell must be adjusted to meet the requirements, for example, temperature restrictions of the silicon bottom cell, which increases the complexity of the device engineering. However, this architecture has the advantage of less lateral current collection in the transparent contact region between the two sub-cells, as only vertical transport is necessary in the interconnecting layer. Therefore, less conductive layers can be employed reducing parasitic absorption. Moreover, a monolithic architecture requires only one substrate support and only one external circuit which also reduces costs. To realize high efficiencies, current matching between the monolithically processed sub-cells needs to be achieved and thus the optical features of the tandem stack become highly important.

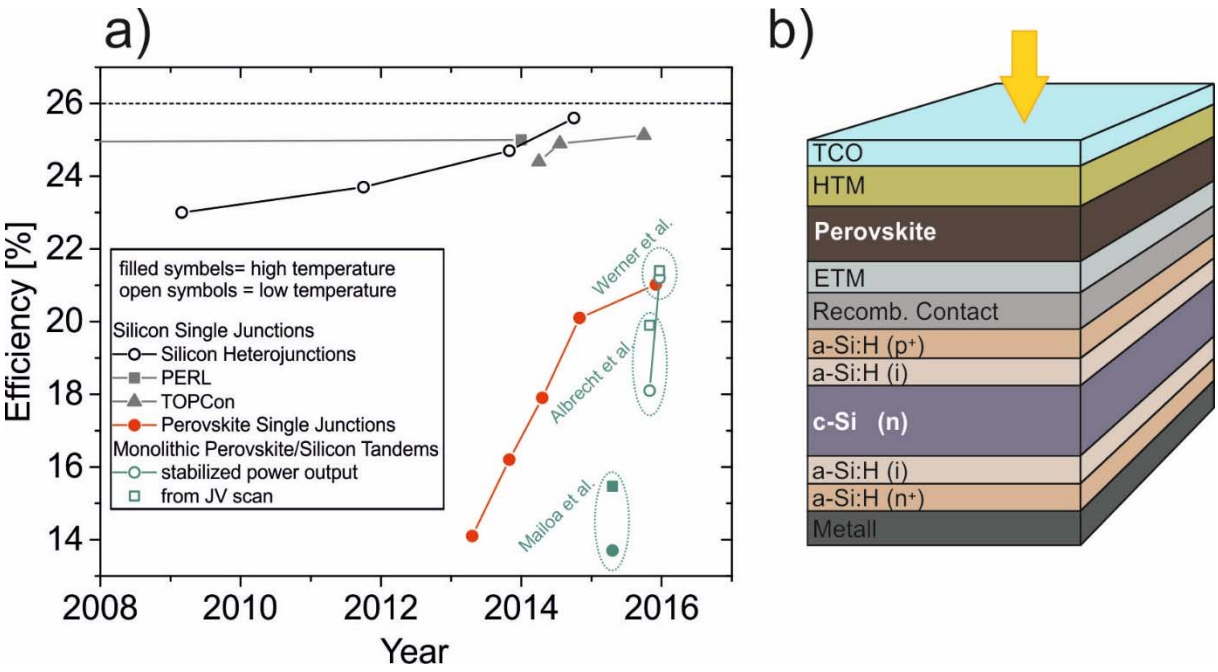

FIG. 1: a) Certified or published record efficiencies over time for various PV technologies including silicon and perovskite single junctions according to Refs[1,2,13,18,19] together with the published monolithic perovskite/ silicon tandem cells according to Refs.[20-22] Filled symbols refer to device designs using >200°C temperature during device processing. Open symbols refer to low temperature (<200°C) processing routes. b) Schematic device design of the

monolithic silicon heterojunction/perovskite tandem solar cell. The visible spectrum of the sunlight is absorbed by the perovskite front-cell and the NIR spectrum by the silicon back-cell.

Figure 1a) displays the evolution in certified power conversion efficiency of different silicon single cell technologies, perovskite single junctions together with non-certified monolithic perovskite/silicon tandem cells that have been published so far.[20-22] All of the displayed silicon technologies show efficiencies around 25% or above. The PERL cell, which held the silicon single junction efficiency record for a long time, was a proof-of-concept device based on expensive manufacturing processes such as photolithography. In contrast, silicon heterojunction cells are economically viable and in production, and at the same time this cell type currently holds the single junction efficiency record, achieved in a rear contact geometry.[13] While this low temperature, plasma deposition based technology is considered to be somewhat disruptive, the TOPcon cell concept is regarded as a possible upgrade path for today's commercial high efficiency cells fabricated on monocrystalline silicon using high temperature diffusion processes. These technologies have been highly optimized and are therefore close to the proposed practical limit of 26%[11,12] (dashed line). Thus, a lot of effort is necessary to overcome this limit with silicon technologies itself. At the same time, when such cells are used as the bottom cells in silicon-based tandem cells, they provide an ideal basis to explore the efficiency limits of such architectures.

An alternative way to produce highly efficient devices is to use a complementary absorber such as perovskites that can be implemented into tandem devices. Since 2013, the efficiency of perovskite single junctions has been increasing steadily, reaching values above 21% at the end of 2015.[1,3] Due to the high efficiency of perovskite single junctions, tandem applications are becoming more and more relevant. Up to now three publications reported on monolithic perovskite/silicon tandem cells with very promising results that are summarized in Figure 1 left. Mailoa, Bailie and coworkers,[20] published the first monolithic perovskite/silicon tandem cell using a diffused silicon homojunction cell with an intermediate tunnel recombination contact

formed by highly n-doped amorphous hydrogenated silicon, which was deposited on the diffused p++ emitter and then partially crystalized in a high temperature step. This silicon bottom cell is temperature stable and therefore a mesoporous TiO_2 scaffold could be used for the perovskite top cell that had silver nanowires as transparent top contact. Their device design showed 15.5% efficiency under reverse scan direction (from open circuit to short circuit conditions) and a stabilized efficiency of 13.7% with a stabilized V_{oc} of 1.58 V. The photocurrent was strongly limited by the parasitic light absorption of the doped spiro-OMeTAD layer.[20]

In our previous work, we developed the first monolithic perovskite/silicon-heterojunction (SHJ) tandem cell using a planar perovskite sub-cell that was processed at temperatures below 120°C.[22] The monolithic integration of the semitransparent perovskite sub-cell on the SHJ starts with an atomic layer deposited SnO_2 grown at low temperatures which functions as energetically aligned electron selective contact.[23] A sandwich consisting of spin-coated spiro-OMeTAD, thermally evaporated MoO_3, and sputtered ITO served as the hole selective transparent top contact. This resulted in a tandem cell efficiency of 19.9% with an open circuit voltage (Voc) of 1.785 V for the reverse scan direction and 18.1% for the stabilized power output measurement. We furthermore showed the proof-of-concept for implementing textured, transparent foils[24] for anti-reflection (AR) and light trapping to enhance the photocurrent that is generated in the silicon bottom cell. Recently, Werner and coworkers realized a monolithic perovskite/silicon-heterojunction tandem cell with the highest efficiency so far.[21] They used an organic electron extraction contact formed by the fullerene derivative PCBM which is known to positively affect the transient effects that result in a reduced hysteretic behavior when measuring the JV curve. Using the same textured foil for improved absorption and AR as in Ref,[22] Werner et al. could realize an efficiency of 21.4 % in forward scan and an only slightly reduced stabilized efficiency of 21.2%. These encouraging results, make the perovskite/silicon

tandem architecture a promising concept to overcome the practical efficiency limit of silicon single-junctions in the near future.

Figure 1b) displays the typical device structure of a silicon heterojunction/perovskite monolithic tandem solar cell that was used in the present work, in our previous publication and by Werner et al.[21,22] High quality surface passivation of the n-type wafer is provided by thin layers of intrinsic (i) amorphous hydrogenated silicon a-Si:H, the front emitter is made from p-doped a-Si:H and the back surface field by n-doped a-Si:H. In this device design, the perovskite top cell can be directly applied in its "normal" configuration with the perovskite being grown on the electron transport material (ETM), e.g. TiO_2, SnO_2, or PCBM, facing towards the recombination contact that interconnects both sub-cells. The top contact is formed by the hole transporting material (HTM), e.g. doped Spiro-OMeTAD and sputtered TCOs or solution processed layers such as silver nanowires[14] or graphene.[17] When using a sputtered TCO, a thin buffer layer of thermally evaporated MoO_3 can be utilized to protect the organic HTM during the sputter process.[25]

Taking a closer look into the optical properties of this device stack it is obvious that a thin multilayer stack with different optical features and, for most layers in the stack, smaller refractive indexes (~2) is formed on top of an optically thick silicon wafer with a high refractive index (~4). Therefore strong interference features and reflection losses occur when flat interfaces are present in the device.

In this work, we summarize the experimental efforts on monolithic perovskite/silicon tandem cells and highlight the importance of the optical optimization of planar monolithic perovskite/silicon tandem cells. We experimentally show the influence of the ITO thickness in the interconnecting layer and fabricate an efficient monolithic tandem cell featuring an ITO layer with reduced thickness, showing slightly improved absorption within the silicon sub-cell as compared to our previous work[22] and a stabilized power output of 17%. Furthermore we

present detailed optical simulations on experimentally relevant planar tandem stacks and model systems to give practical guidelines for further device optimizations. By optimizing the thickness of the functional and the perovskite absorber layers, together with the optimization of the perovskite band-gap, we present a tandem stack that can yield ca. 17.5mA/cm² current at a 1.73 eV band-gap. This would translate into an efficiency of over 28% for the monolithic perovskite/silicon-heterojunction tandem solar cell under the realistic assumption of 81% fill factor for the tandem cell and an open circuit voltage of 2.0 V with contribution of 1.3 V from perovskite and 0.71 V from the silicon bottom cell.

METHODS

Tandem solar cell fabrication: The experimental details on the tandem cell fabrication can be found elsewhere.[22] Briefly, both-side polished float zone n-type (111) oriented wafers with 4 inch diameter, 255 µm thickness, and a resistivity of 2-5 Ω·cm were cleaned with the standard RCA process and etched for 1 minute in diluted hydrofluoric acid immediately before a-Si:H deposition. Intrinsic a-Si:H layers were deposited by standard PECVD processes using silane, as precursor gas. The n-type and p-type doped a-Si:H layers were prepared by adding PH_3 or B_2H_6 to the precursor gas, respectively. On the front side of the wafer, 40, 60 or 80 nm ITO was deposited by RF magnetron sputter deposition in a Roth & Rau sputter tool at room temperature. The back contact was formed by sputtering 70 nm of aluminum doped zinc oxide (AZO) and 400 nm silver in a Leybold Optics A600V7 tool at room temperature. After finishing the back contact, the silicon samples were annealed at 200°C for 5 min in air.

15 nm-SnO_2 layers were deposited at 118 °C using nitrogen as a carrier gas Tetrakis(dimethylamino)tin(IV) (TDMASn) and ozone. TDMASn was held at 65 °C and ozone was produced by an ozone generator fed with oxygen gas. The perovskite precursor solution contained FAI (1 M), PbI2 (1.1 M), MABr (0.2 M) and PbBr2 (0.2 M) dissolved in anhydrous DMF:DMSO 4:1 (v:v). The perovskite solution was spin coated in a two steps program at 1000

and 6000 rpm for 10 and 30 s, respectively. During the second step, 200 µL of chlorobenzene was poured on the spinning substrate 15 s prior to the end of the program. The substrates were then annealed at 100°C for 1h in a nitrogen filled glove box. A spiro-OMeTAD solution (70 mM in chlorobenzene) doped with Li-TFSI, FK209 and TBP was spin coated at 4000 rpm for 20 s. The molar ratio of additives for spiro-OMeTAD was: 0.5, 0.03 and 3.3 for Li-TFSI, FK209 and TBP respectively. A 27 nm thick MoO_3 buffer layer was thermally evaporated on top of the spiro-OMeTAD layer and finally, the top contact was formed by 80 nm ITO deposited by DC magnetron sputtering without further annealing of the sample.

Measurements: JV measurements were conducted using a "Steuernagel Lichtechnik" sun simulator, mimicking AM 1.5G spectra and adjusted to 100 mW/cm² by measuring the short circuit current of a calibrated silicon solar cell (Fraunhofer ISE). The silicon reference and the monolithic tandem samples were temperature controlled to 25°C during measurement. The monolithic tandem cell has an active area of 4x4 mm² defined by both ITO layers and an 3 x3 mm² aperture was used during JV measurement. The EQE was measured with monochromated light from a dual source lamp (tungsten or halogen) mechanically chopped to 78 Hz for the detection with a lock-in amplifier. The intensity of the lamp is checked with calibrated reference diodes. Constant background illumination was provided by 450 nm LED light or a halogen lamp filtered with an RG 850 edge filter. Transmission and reflection spectra were measured with a PerkinElmer UV−VIS spectrometer, equipped with an integrating Ulbricht sphere and calibrated using a Fraunhofer ISE certified white standard.

Optical simulations: The optical simulations of the tandem stacks presented in figure 4 were conducted using a transfer matrix algorithm implemented in the software "GenPro4",[26] which was developed at the Delft University of Technology. The optically thick c-Si layer was treated to be non-coherent in the simulation as the coherence length of sunlight is much smaller than the layer thickness of 250 µm. As input to the simulations, optical data (n,k) of the layers were

either extracted from spectral ellipsometry measurements or taken from literature for spiro-OMeTAD[5], perovskite,[27] MoO_3,[28,29] and (n)nc-Si:H,[30] respectively. The optical parameters of the higher band-gap perovskites have been generated by shifting the optical constants from Ref[27] in 20 nm steps into the blue. Note that recent experimental findings on higher band-gap perovskites agree with a complete blue-shift of the absorption coefficient as utilized here.[7] We performed the thickness optimization with the *simulated annealing* algorithm,[31] a Monte Carlo method as it is implemented in the MATLAB Global Optimization Toolbox. During the optimization, all the layers above the (p) a-Si:H were allowed to vary in thickness within the experimental relevant parameter range (see Table 2). As a cost function we used the minimum of the maximum achievable current densities in the top and bottom cells, which was maximized. The maximum achievable current density is calculated by multiplication of the simulated absorption with wavelength and the photon flux according to the AM 1.5G spectrum. The resulting spectrum is then integrated over wavelength from 350 to 1200 nm. Thus, with the absorption of the functional layers and the total reflection, the parasitic absorption and reflection can be correlated to a current density loss. Note that the maximum achievable current is comparable to the short circuit current (Jsc) under the assumption that 1) the sub-cells are close to current matching and 2) all photons absorbed in the individual sub-cell at the respective wavelength range generate charges that can be collected at short circuit conditions. The later assumption can hold for both, the silicon-heterojunction[32] and the perovskite[33] materials.

The Voc of the sub-cells in the tandem stack was estimated by the logarithmic dependence of Voc on the photocurrent density.[34] From the Voc of typical perovskite and c-Si single-junctions, the reduced Voc found in the tandem stack for the respective sub-cell was evaluated. The silicon sub-cell is reduced by 21 mV when the Jsc is reduced from that of the single-junction around 40 mA/cm² to 17.5 mA/cm² in the tandem stack. The Voc of the perovskite sub-cell is only

slightly affected. When reducing from ~21 mA/cm² as found in single junction devices to 17.5 mA/cm² in the optimized tandem, the Voc decreases by only 6 mV.

RESULTS

Figure 2a shows simulated transmission and reflection spectra of tandem devices that have the general architecture as shown Figure 1b) with an ITO/SnO_2 intermediate contact as used in our previous work,[22] but with a varied c-Si layer thickness and no metallic back electrode. It can be seen that the interference features within the reflectance spectra are predominantly caused by the layer stack of the thin perovskite sub-cell on top of the thick c-Si wafer. Only when the transmission through the 250µm thick wafer is significantly increased for wavelength above 1000 nm, the range in which the c-Si becomes more transparent, the reflection of the 250 µm thick c-Si changes as compared to the semi-infinite c-Si slab in the tandem configuration. Thus, to eliminate the reflectance features in the spectral range below 1000 nm, which cause optical losses, it is necessary to optically optimize the perovskite sub-cell and its functional layers. Any light trapping schemes that are applied at the back of the silicon wafer will only enhance the EQE at the onset of the silicon sub-cell absorption, thus in the range above 1000 nm.

By utilizing optical simulations, we have proposed in our previous work that the ITO in the intermediate contact significantly alters the optical features within the monolithic tandem stack.[22] To further proof this experimentally, we have fabricated monolithic tandem devices that have different ITO thicknesses ranging from 40 to 80 nm without altering the other layers. The general device architecture is similar to that of our previous publication.[22] Figure 2b) displays experimental results of the EQE and the reflection with different ITO thicknesses in the recombination contact. It is obvious that the thickness of the intermediate ITO layer is not affecting the reflection and EQE in the range where the perovskite absorbs, but that of the silicon in the range between 800 and 1150 nm. Reducing the ITO thickness strongly reduces the reflection at 900 nm, and the current that can be generated by the silicon sub-cell in the

range between 750 and 1200 nm increases by 0.8 mA/cm² for 40 nm ITO, as compared to the 80-nm thick case. Note that we found in the experiment that the enhanced EQE below 730 nm might be slightly affected by partial shunts and thus changes with different bias light intensity. Therefore this range is not not used for the integration.

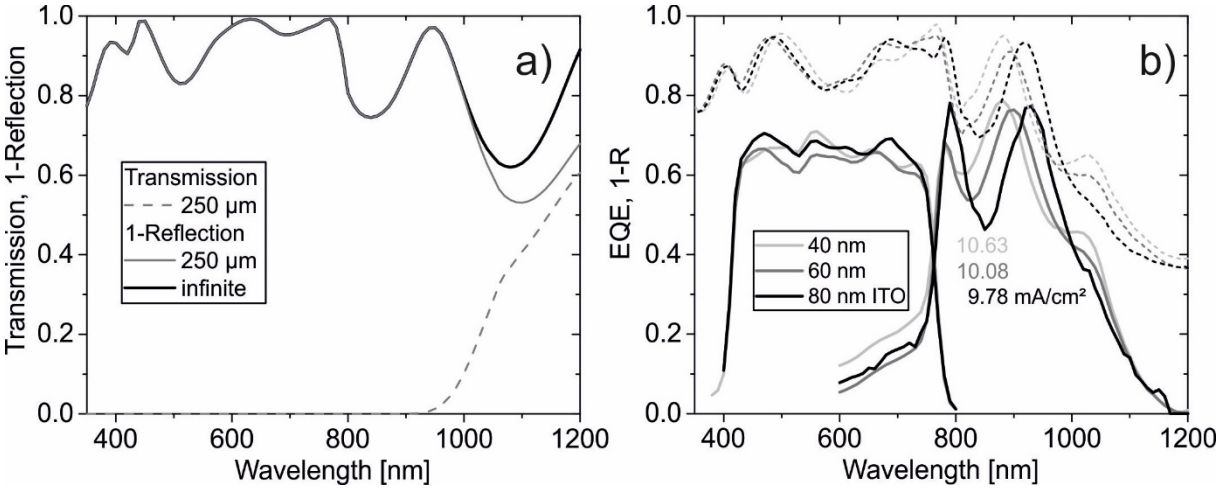

FIG. 2 a): Simulated reflection and transmission of model tandem device stacks with the general architecture shown in Figure 1b) but without a metallic back contact. The reflection is shown for devices with either 250 µm thick c-Si (as used in the experiment) or semi-infinite thick c-Si slab. The transmission shows the light that passes through the back side of the 250 µm thick c-Si. b) Experimental reflection and external quantum efficiency (EQE) of the individual sub-cells in monolithic tandem devices w/o AR coating as function of ITO thickness within the intermediate recombination contact. Also shown is the current from multiplication of the EQE with wavelength and the AM 1.5G spectra and integration over the wavelength range 750-1200 nm.

Further reduction of the reflectance losses is possible using an LiF layer as a second , additional AR coating,[20] which has an refractive index in between that of air and ITO. We used the monolithic tandem cell with 40 nm ITO intermediate layer from Figure 2b) and evaporated LiF to reduce reflection and enhance EQE. Figure 3a shows the resulting JV curves under simulated AM 1.5G illumination calibrated to 100 mW/cm² when scanning in forward and reverse direction. The inset shows the current density and efficiency at a fixed voltage close to the maximum power point measured over a period of 50 sec. The corresponding performance data can be found in Table 1. Figure 3b) displays the EQE of the two sub-cells in the monolithic tandem configuration accessed with bias light.

Due to hysteresis effects, the JV reverse scan (from Voc to Jsc) results in higher FF of 75.3% and Voc of 1780 mV as compared to the forward scan. Holding the cell for several seconds at the maximum power point deduced from the reverse scan, the efficiency stabilizes at ca. 17% after 40 sec. The measured Jsc of 14 mA/cm² matches the photocurrent obtained by integration of the EQE that results in 14.3 mA/cm² for the silicon bottom cell. This is slightly higher as compared to our previous result.[22] However, the photocurrent density gained from the perovskite top-cell is by 2.4 mA/cm² higher and therefore the non-matched JV curve is strongly limited by the silicon bottom cell.

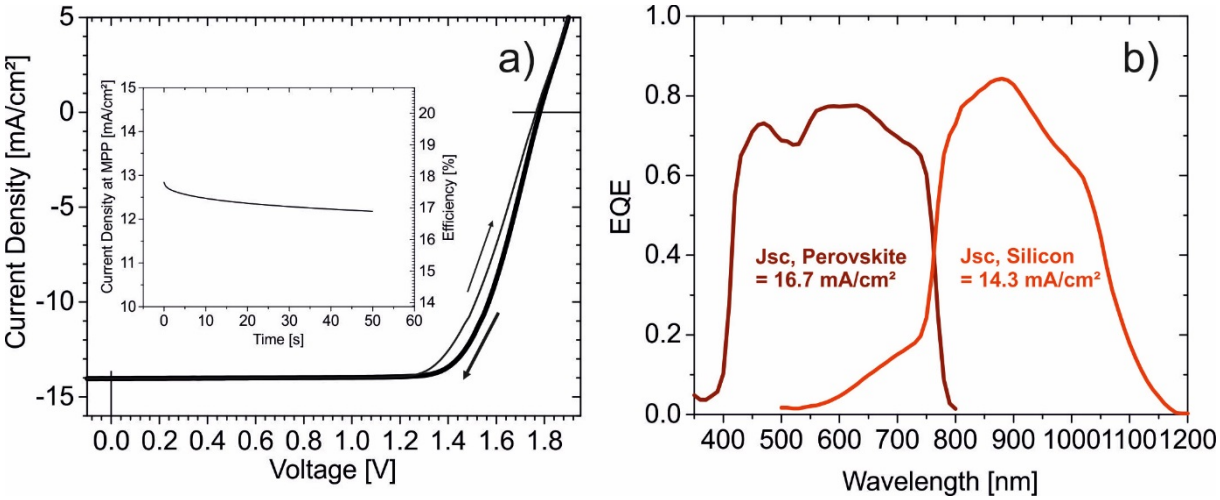

FIG. 3: a) *JV* characteristics of a monolithic tandem device with AR coating and 40 nm thick intermediate ITO measured at a scan rate of 500 mV/s in forward and reverse scan (as indicated by the arrows). The inset shows the photocurrent and the efficiency as a function of time at a fixed applied voltage close to the MPP. b) External quantum efficiency (EQE) of the individual sub-cells of the device in a).

Table 1: Performance data from EQE and JV measurements of the monolithic tandem presented in Figure 3. The current from EQE is deduced as described in methods section. Due to hysteresis, different bias scanning directions were used at a scan rate of 500 mV/s for measuring the JV characteristics. The stabilized power output was obtained from holding the cell close to maximum power point (fixed bias) and measuring the current as a function of time.

measurement	J_{sc} [mA/cm²]	V_{oc} [mV]	FF [%]	PCE [%]
EQE (perovskite/silicon)	16.7 / 14.3			
JV reverse (V_{oc} to J_{sc}) scan	14.03	1780	75.3	18.8
JV forward (J_{sc} to V_{oc}) scan	14.03	1760	72.3	17.9
efficiency at MPP after 40 sec				17

To further improve the device architecture, current matching must be realized and the reflectance losses should be reduced. Therefore, we simulated a thickness variation of the perovskite top-cell and its functional layers and calculated the photocurrent of the limiting sub-cell for different device designs as shown in figure 4 within the experimental thickness range presented in table 2. For the optimization, we used the simulated annealing algorithm as described in the methods section. During an optimization run, several thousands of different layer thickness combinations for each tandem architecture are evaluated using GenPro4 to find the maximal achievable photocurrent density that can be realized with a particular layer stack. In table 2, the optimized thicknesses together with the absorption loss of each layer can be found for the three different device designs.

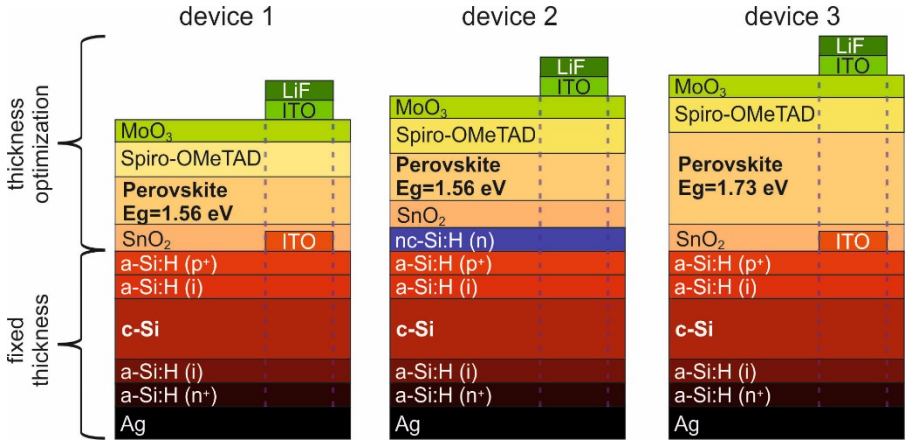

FIG. 4: Schematic representation of the simulated device structure that was used in Figure 5 and 6. Three different devices designs were simulated and optimized to reach the highest Jsc in the tandem structure: device 1 is that used in the experiment, device 2 instead of ITO uses an n-type nc-Si:H layer as recombination contact and device 3 uses the experimental contact design but a perovskite with optimized optical band-gap. For film thicknesses see Table 2.

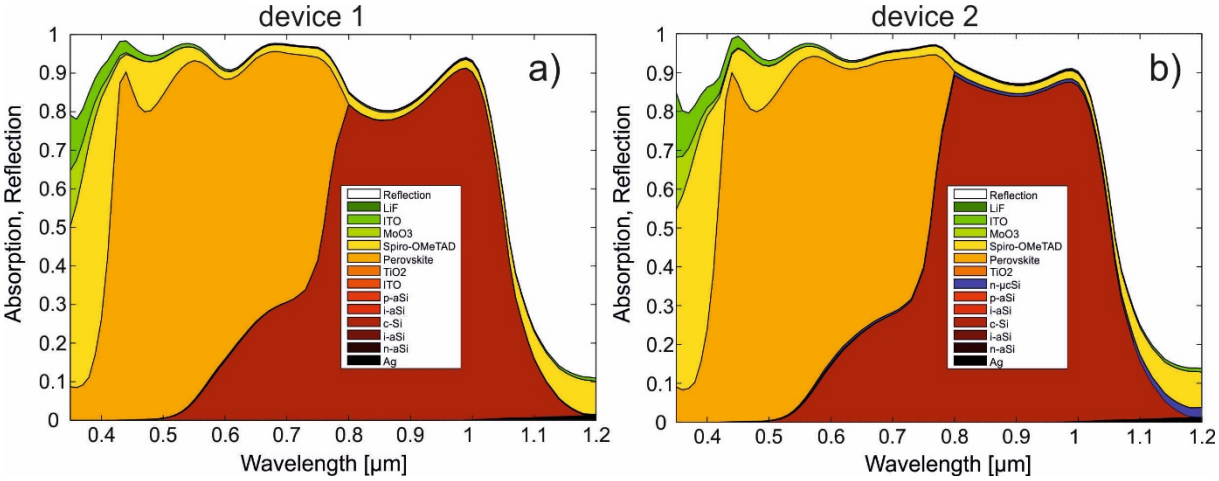

FIG. 5: Breakdown of absorption and reflection vs. wavelength from simulations of monolithic tandem cells under illumination in normal incidence, in which all thicknesses of the perovskite sub-cell and the contact layers have been optimized in experimental relevant thickness ranges to get the highest photocurrent density close to current matching. a): monolithic tandem cell with an ITO contact as intermediate recombination layer. b): intermediate recombination layer formed by a direct junction of n-type nc-Si:H with the p-type emitter of the bottom cell. For film thicknesses see Table 2.

Table 2: Simulated photocurrent and optimized thicknesses of the individual layers that yield the highest current density of the limiting sub-cell. The photocurrent and reflection loss is deduced from the simulated absorption shown in Figure 5 and 6. Additionally, the experimentally relevant layer thickness range is given that was used as boundary conditions for the optimization. Device 1 is shown in Figure 5a) and contains an ITO intermediate recombination contact, device 2 (Figure 5b) contains n-type nc-Si:H, and device 3 (Figure 6a) contains the optimized band-gap and an ITO recombination contact.

Layer	Photocurrent, Device 1 [mA/cm²]	Thickness Device 1 [nm]	Photocurrent, Device 2 [mA/cm²]	Thickness Device 2 [nm]	Photocurrent, Device 3 [mA/cm²]	Thickness Device 3 [nm]	Thickness Range [nm]
Reflection	7.77		7.20		8.17		
LiF	0	101	0	108	0	93	0 - 200
front ITO	0.36	103	0.4	115	0.32	87	60 - 150
MoO3	0.16	30	0.14	25	0.16	26	20 - 40
spiro-OMeTAD	2.63	151	2.64	155	2.41	133	120 - 300
perovskite*	**17.52**	291(1.56 eV)	**17.65**	326(1.56 eV)	**17.48**	1386(1.73 eV)	200 - 1500
TiO2	0.01	11	0.01	10	0.02	16	10 - 20
middle ITO	0.01	26	-	-	0.01	20	20 - 100
n µc Si:H	-	-	0.32	29	-	-	20 - 100
p a-Si:H	0.02	8	0.02	8	0	8	8
i a-Si:H	0.02	5	0.02	5	0	5	5

c-Si	**17.52**	250µm	**17.64**	250µm	**17.47**	250µm	250 µm
i a-Si:H	0	5	0	5	0	5	5
n a-Si:H	0	8	0	8	0	8	8
Ag	0.06	Inf.	0.06	Inf.	0.06	Inf.	Inf.

***** the optical band-gap of the perovskite used in the simulation is indicated in brackets in eV.

Figure 5 displays the simulated absorption of each layer in the tandem stack. In the plot, the absorption of each layer is summed up at each wavelength to directly illustrate the parasitic absorption and reflection losses. Table 2 shows the maximum achievable photocurrent density that can be gained as defined in the methods section. The simulation reveals that starting from a perovskite thickness of 600 nm and not optimizing the functional layers, results in highly imbalanced photocurrent densities of 20 mA/cm² for the perovskite and only 13 mA/cm² for the silicon sub-cell (data not shown). Reducing the perovskite thickness to 300 nm, for higher transmission of red photons into the silicon enhances the photocurrent to ~15 mA/cm² in the silicon sub-cell. When in addition, the functional layers are optimized to meet current matching, current densities above 17 mA/cm² can be realized in both sub-cells.

Figure 5a) displays the absorption of the individual layers when a 290 nm thick perovskite layer and an intermediate ITO thickness (device 1) of 26 nm is simulated, which is even lower than used in the experiment. At this thickness combination, the maximum achievable photocurrent density can be matched at 17.5 mA/cm² even in the absence of any additional light trapping scheme. By replacing the intermediate ITO with n-doped nc-Si:H (Figure 5b, device 2) that can act as efficient tunnel recombination contact with the p-type emitter, the reflection can be slightly decreased as compared to the ITO based sample and therefore photocurrents of 17.65 mA/cm² are possible. Generally, thicker nc-Si:H layers resulted in lower reflection but enhanced parasitic absorption in that layer. The simulations also showed that the reflection reduction depends on the refractive index of the recombination contact. By using more transparent nanocrystalline silicon oxide (nc-SiOx:H),[35] the reflection at thicker layers (60-80 nm) can be reduced, at the same time leading to reduced parasitic absorption. It is known

that by tuning the silicon to oxygen ratio, the refractive index of this layer can be manipulated. This can be utilized to reduce of the total reflection of the tandem stack further. However, a photocurrent density above 17.5 mA/cm² in both sub-cells and a photocurrent loss of 2.5 mA/cm² in spiro-OMeTAD means an overall photocurrent density above 37.5 mA/cm², which is close to the maximum photocurrent density that can be collected from the solar spectrum up to 1200 nm including typical reflection losses in planar structures. Thus, significant enhancements in photocurrents are not likely when not exchanging the functional layers e.g. spiro-OMeTAD that show parasitic absorption and by implementing light trapping to reduce the reflection and to enhance the EQE at the absorption onset of the c-Si.

It was proposed, that the optimal band-gap of the perovskite when combined with c-Si in a tandem cell is around 1.74eV,[7] which is in agreement with calculations based on the detailed balance limit for tandem cells with different optical band-gaps.[36] Recently, some of the authors of this work demonstrated that a photostable perovskite based on mixtures of cesium and formamidinium as well as iodide and bromine can be employed to tune the band-gap to 1.74 eV enabling a high Voc of 1.2 eV.[7]

To the best of our knowledge no device relevant simulations were carried out so far, showing the optimized optical band-gap that yields the highest device efficiencies in monolithic perovskite/c-Si tandem cells with experimentally relevant parameters. Thus in Figure 6b) we perform simulations with different perovskite band-gaps. For each band-gap the current-matched Jsc is optimized via the thickness optimization routine already used in Figure 4. Furthermore, based on the experimentally found Voc of 1.13V in single junction configuration, which has been shown for $CH_3NH_3PbI_3$ based devices with EQE onsets around 800 nm,[37,38] the Voc of the perovskite sub-cells with higher band gaps is estimated. Here we assume that the higher energy of the optical band-gap directly translates into a higher Voc. However we include a slight decrease of Voc in the tandem cell of 6mV due to the reduced photocurrent generation

as compared to the single junction configuration (see methods section). When increasing the band gap from 1.56 eV towards 1.7 eV in the simulation, the Jsc of the tandem cell is not altered, as the optimized thickness for the higher band-gap perovskite increases in parallel. Therefore, the absorption onset of the perovskite is sharper and less photons above the perovskite band-gap are transmitted to the silicon for higher band-gaps, leaving the sum of photocurrents of both sub-cells unchanged. This is indicated by the white and grey lines in Figure 6a). Further increasing the band-gap well above 1.7 eV will get into limitation of the perovskite absorption also for very thick perovskite films with a thickness above 1500 nm, which was set as the maximum experimentally relevant thickness in the simulation (indicated by the dashed line in Figure 6b). Note that efficient devices with thicknesses up to 3µm were shown recently by utilizing blade coating,[39] and the typical charge carrier diffusion length in perovskites is in the order of micrometer.[40,41] However further increasing the perovskite thickness from 1.5 to 3µm for a band gap of 1.78 eV did not significantly enhance the tandem Jsc. Thus, the optimum between high Jsc and high Voc is found for a band-gap of 1.73 eV (corresponding to an absorption onset of 715 nm) for which 17.48 and 17.47 mA/cm² can be generated in the perovskite and silicon sub-cell, respectively (see Table 2). Assuming to have a silicon-heterojunction Voc of 730 mV in single junction configuration, the Voc in the bottom cell can be reduced by 21 mV according to the reduced Jsc in the tandem (see methods section). By further assuming an FF of 81% which is just slightly above the experimentally record value (data not shown), efficiencies of the tandem device are found to be 28.4% for the optimized band gap.

Figure 6a) displays the absorption and reflection together with the current that can be generated in each layer and the loss current due to reflection for a simulated tandem cell with the optimized band-gap of 1.73 eV and 1383 nm perovskite thickness (device 3). For thicker perovskite layers, the absorption edge at the perovskite band-gap is very sharp and therefore enables to have

current matching at higher band-gaps. In addition, the number of interference fringes increases and with that the overall reflection loss is slightly enhanced (see Table 2) for thicker perovskite layers.

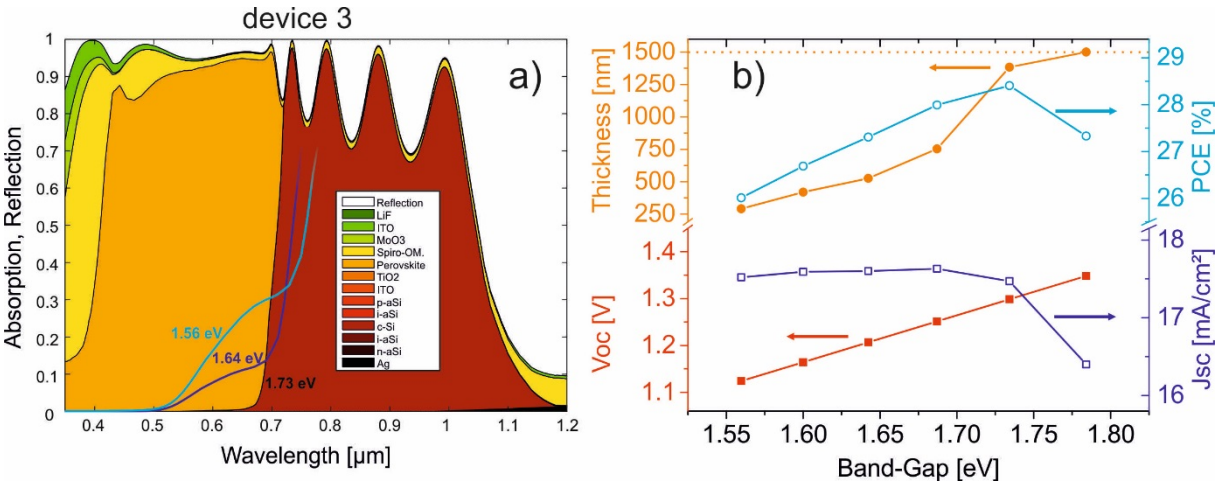

FIG. 6: a) Breakdown of absorption and reflection vs. wavelength from simulations of monolithic tandem cells under illumination in normal incidence, with an ITO intermediate layer and with an optimized perovskite band-gap of 1.73eV. The thickness of all top-cell layers was optimized within the thickness range presented in Table 2 to realize the highest photocurrent density. The light and dark blue lines show the absorption onset of the perovskite sub-cell tandem stacks with perovskite band-gaps of 1.56 eV and 1.64 eV as indicated. b) Left scale: Voc and optimized film thickness of the perovskite sub-cell. Right scale: Jsc and tandem cell efficiency as a function of the used perovskite band-gap. For the efficiency calculation a FF of 81% and a silicon Voc of 709 mV in tandem geometry was assumed.

DISCUSSION

We can draw a clear strategy to further enhance the performance of monolithic perovskite/silicon tandem solar cells. First, experimental routes to fabricate stable perovskites with the optimized band-gap of around 1.73 eV must be identified which may be provided by cation mixtures of cesium and formamidinium and halide mixtures of bromide and iodide.[7] Second, the open circuit voltage of the higher band-gap perovskites needs to be increased to around 1.3 V. Therefore depending on the energy level shifts accompanied with the band-gap enhancement, new charge carrier selective materials with fine-tuned energetics need to be applied to make sure that the Voc is not contact limited. Third, the perovskite layer thickness at the optimized band-gap should be enhanced to values above 1µm to make sure that the light

between 500 to 700 nm is fully absorbed in the perovskite. With these three ingredients, the efficiency can be boosted to values above 28%. Fourth, the parasitic absorption of the spiro-OMeTAD layer between 350 and 730 nm is in the order of 1.8 mA/cm². Especially for the optimized band-gap, reducing this current loss could be directly translated into higher photocurrent generation in the perovskite, provided it becomes possible to either process the spiro-OMeTAD layer much thinner or other hole transporting materials with less parasitic absorption are found. To circumvent this parasitic absorption also, inverted perovskite architectures are highly favorable as electron selective window layers such as PCBM or ZnO can be applied that show less parasitic absorption and enhanced stability.[42,43] Fifth, for the thicker perovskite with the optimized band-gap, the interference and accompanying reflection losses could be significantly decreased when applying light trapping schemes either at the back side of the wafer or on the front of the planar top-contact. In addition, if strategies can be developed that allow for conformal growth of the perovskite on textured silicon wafers, the standard silicon texture processing could be utilized that enables highly efficient light trapping in the silicon.

CONCLUSION

In conclusion, we reported on the optical optimization of planar monolithic silicon heterojunction/perovskite tandem solar cells and showed a clear strategy for further device optimization. In particular, experimentally reducing the intermediate ITO thickness resulted in slightly enhanced absorption in the limiting silicon bottom-cell. Thus, a 17% efficient monolithic tandem cell was fabricated with the reduced intermediate ITO thickness that exhibits a non-matched current of 16.7 mA/cm² versus 14.3 mA/cm² in the perovskite and silicon sub-cell, respectively. To further optimize the current matching, we performed optical simulations in which all film thicknesses of the top-cell and its functional layers were optimized to gain the highest photocurrent density. We have shown that the optimum layer thickness combination is

different from the experiment, and it should be possible to produce almost the same photocurrent density of 17.5 mA/cm² and 17.6 mA/cm² for devices with a thin ITO recombination contact (device 1) or instead using n-type nc-Si:H (device 2), respectively. We further studied the increase of the perovskite band-gap on the tandem performance in detail and found the optimum band-gap for this device architecture to be around 1.73 eV (device 3), including experimentally relevant parameters and the typical parasitic absorption of spiro-OMeTAD. At this perovskite band-gap, the Voc should be enhanced to 1.3 V, provided that the energetic increase in band-gap can be directly translated into a higher Voc. Together with the assumption of having a FF of 81%, this would result in a planar monolithic tandem cell with an efficiency of 28.4%. Further work will be devoted to finding optimal light trapping schemes that enable efficient light management in this fascinating type of tandem architecture.

ACKNOWLEDGEMENTS

The authors would like to thank Thomas Lußky, Erhard Conrad, Kerstin Jacob, Tobias Hänel, and Karolina Mack from HZB as well as Manuel Hartig from TU Berlin for technical assistance. S.A. acknowledges Simon Kirner from PVcomB and Marko Jost from University of Ljubljana for fruitful discussions. Further, Rudi Santbergen from Delft University of Technology is acknowledged for providing GenPro4. Financial support was provided by the European Union Seventh Framework Programme (FP7) through the MESO project (grant no. 604032) and by the Helmholtz-Gemeinschaft through the joint project Hi-ERN.

REFERENCES

(1) http://www.nrel.gov/ncpv/images/efficiency_chart.jpg, accessed 01-03-2015.

(2) Yang, W. S.; Noh, J. H.; Jeon, N. J.; Kim, Y. C.; Ryu, S.; Seo, J.; Seok, S. I. *Science* **2015**, *348*, 1234.

(3) Bi, D.; Tress, W.; Dar, M. I.; Gao, P.; Luo, J.; Renevier, C.; Schenk, K.; Abate, A.; Giordano, F.; Correa Baena, J.-P.; Decoppet, J.-D.; Zakeeruddin, S. M.; Nazeeruddin, M. K.; Grätzel, M.; Hagfeldt, A. *Science Advances* **2016**, *2*.

(4) Saliba, M.; Matsui, T.; Seo, J.-Y.; Domanski, K.; Correa-Baena, J.-P.; Mohammad K, N.; Zakeeruddin, S. M.; Tress, W.; Abate, A.; Hagfeldt, A.; Gratzel, M. *Energy & Environmental Science* **2016**, DOI: 10.1039/C5EE03874J.

(5) Filipič, M.; Löper, P.; Niesen, B.; De Wolf, S.; Krč, J.; Ballif, C.; Topič, M. *Optics Express* **2015**, *23*, A263.

(6) Loper, P.; Moon, S.-J.; Martin de Nicolas, S.; Niesen, B.; Ledinsky, M.; Nicolay, S.; Bailat, J.; Yum, J.-H.; De Wolf, S.; Ballif, C. *Physical Chemistry Chemical Physics* **2015**, *17*, 1619.

(7) McMeekin, D. P.; Sadoughi, G.; Rehman, W.; Eperon, G. E.; Saliba, M.; Hörantner, M. T.; Haghighirad, A.; Sakai, N.; Korte, L.; Rech, B.; Johnston, M. B.; Herz, L. M.; Snaith, H. J. *Science* **2016**, *351*, 151.

(8) Shockley, W.; Queisser, H. J. *Journal of Applied Physics* **1961**, *32*, 510.

(9) Loper, P.; Niesen, B.; Soo-Jin, M.; Martin de Nicolas, S.; Holovsky, J.; Remes, Z.; Ledinsky, M.; Haug, F. J.; Jun-Ho, Y.; De Wolf, S.; Ballif, C. *Photovoltaics, IEEE Journal of* **2014**, *4*, 1545.

(10) Lal, N. N.; White, T. P.; Catchpole, K. R. *Photovoltaics, IEEE Journal of* **2014**, *4*, 1380.

(11) Smith, D. D.; Cousins, P.; Westerberg, S.; De Jesus-Tabajonda, R.; Aniero, G.; Yu-Chen, S. *Photovoltaics, IEEE Journal of* **2014**, *4*, 1465.

(12) Swanson, R. M. In *Photovoltaic Specialists Conference, 2005. Conference Record of the Thirty-first IEEE* 2005, p 889.

(13) Masuko, K.; Shigematsu, M.; Hashiguchi, T.; Fujishima, D.; Kai, M.; Yoshimura, N.; Yamaguchi, T.; Ichihashi, Y.; Mishima, T.; Matsubara, N.; Yamanishi, T.; Takahama, T.; Taguchi, M.; Maruyama, E.; Okamoto, S. *Photovoltaics, IEEE Journal of* **2014**, *4*, 1433.

(14) Bailie, C. D.; Christoforo, M. G.; Mailoa, J. P.; Bowring, A. R.; Unger, E. L.; Nguyen, W. H.; Burschka, J.; Pellet, N.; Lee, J. Z.; Gratzel, M.; Noufi, R.; Buonassisi, T.; Salleo, A.; McGehee, M. D. *Energy & Environmental Science* **2015**, *8*, 956.

(15) Werner, J.; Dubuis, G.; Walter, A.; Löper, P.; Moon, S.-J.; Nicolay, S.; Morales-Masis, M.; De Wolf, S.; Niesen, B.; Ballif, C. *Solar Energy Materials and Solar Cells* **2015**, *141*, 407.

(16) Werner, J.; Moon, S. J.; Loper, P.; Walter, A.; Filipic, M. In *EU PVSEC 2015* Hamburg, 2015.

(17) Lang, F.; Gluba, M. A.; Albrecht, S.; Rappich, J.; Korte, L.; Rech, B.; Nickel, N. H. *J Phys Chem Lett* **2015**, *6*, 2745.

(18) Taguchi, M.; Yano, A.; Tohoda, S.; Matsuyama, K.; Nakamura, Y.; Nishiwaki, T.; Fujita, K.; Maruyama, E. *Photovoltaics, IEEE Journal of* **2014**, *4*, 96.

(19) Glunz, S. W.; Feldmann, F.; Richter, A.; Bivour, M.; Reichel, C.; Steinkemper, H.; Benick, J.; Hermle, M. In *31st European Photovoltaic Solar Energy Conference and Exhibition, Hamburg* 2015.

(20) Mailoa, J. P.; Bailie, C. D.; Johlin, E. C.; Hoke, E. T.; Akey, A. J.; Nguyen, W. H.; McGehee, M. D.; Buonassisi, T. *Applied Physics Letters* **2015**, *106*, 121105.

(21) Werner, J.; Weng, C.-H.; Walter, A.; Fesquet, L.; Seif, J. P.; De Wolf, S.; Niesen, B.; Ballif, C. *The Journal of Physical Chemistry Letters* **2015**, 161.

(22) Albrecht, S.; Saliba, M.; Correa Baena, J. P.; Lang, F.; Kegelmann, L.; Mews, M.; Steier, L.; Abate, A.; Rappich, J.; Korte, L.; Schlatmann, R.; Nazeeruddin, M. K.; Hagfeldt, A.; Grätzel, M.; Rech, B. *Energy Environ. Sci.* **2016**, *9*, 81.

(23) Correa Baena, J. P.; Steier, L.; Tress, W.; Saliba, M.; Neutzner, S.; Matsui, T.; Giordano, F.; Jacobsson, T. J.; Srimath Kandada, A. R.; Zakeeruddin, S. M.; Petrozza, A.; Abate, A.; Nazeeruddin, M. K.; Grätzel, M.; Hagfeldt, A. *Energy Environ. Sci.* **2015**, *8*, 2928.

(24) Ulbrich, C.; Gerber, A.; Hermans, K.; Lambertz, A.; Rau, U. *Progress in Photovoltaics: Research and Applications* **2013**, *21*, 1672.

(25) Kranz, L.; Abate, A.; Feurer, T.; Fu, F.; Avancini, E.; Löckinger, J.; Reinhard, P.; Zakeeruddin, S. M.; Grätzel, M.; Buecheler, S.; Tiwari, A. N. *The Journal of Physical Chemistry Letters* **2015**, 2676.

(26) Santbergen, R.; Smets, A. H. M.; Zeman, M. *Optics Express* **2013**, *21*, A262.

(27) Loper, P.; Stuckelberger, M.; Niesen, B.; Werner, J.; Filipic, M.; Moon, S. J.; Yum, J. H.; Topic, M.; De Wolf, S.; Ballif, C. *J. Phys. Chem. Lett.* **2015**, *6*, 66.

(28) Roland, S.; Neubert, S.; Albrecht, S.; Stannowski, B.; Seger, M.; Facchetti, A.; Schlatmann, R.; Rech, B.; Neher, D. *Advanced Materials* **2015**, *27*, 1262.

(29) Albrecht, S.; Grootoonk, B.; Neubert, S.; Roland, S.; Wördenweber, J.; Meier, M.; Schlatmann, R.; Gordijn, A.; Neher, D. *Solar Energy Materials and Solar Cells* **2014**, *127*, 157.

(30) Ding, K.; Kirchartz, T.; Pieters, B. E.; Ulbrich, C.; Ermes, A. M.; Schicho, S.; Lambertz, A.; Carius, R.; Rau, U. *Solar Energy Materials and Solar Cells* **2011**, *95*, 3318.

(31) Kirkpatrick, S.; Gelatt, C. D.; Vecchi, M. P. *Science* **1983**, *220*, 671.

(32) Holman, Z. C.; Descoeudres, A.; De Wolf, S.; Ballif, C. *Photovoltaics, IEEE Journal of* **2013**, *3*, 1243.

(33) Yang, B.; Dyck, O.; Poplawsky, J.; Keum, J.; Puretzky, A.; Das, S.; Ivanov, I.; Rouleau, C.; Duscher, G.; Geohegan, D.; Xiao, K. *Journal of the American Chemical Society* **2015**, *137*, 9210.

(34) Wurfel, U.; Neher, D.; Spies, A.; Albrecht, S. *Nat Commun* **2015**, *6*.

(35) Mazzarella, L.; Kirner, S.; Stannowski, B.; Korte, L.; Rech, B.; Schlatmann, R. *Applied Physics Letters* **2015**, *106*, 023902.

(36) Vos, A. D. *Journal of Physics D: Applied Physics* **1980**, *13*, 839.

(37) Shao, Y.; Yuan, Y.; Huang, J. *Nature Energy* **2016**, *1*, 15001.

(38) Tao, C.; Neutzner, S.; Colella, L.; Marras, S.; Srimath Kandada, A. R.; Gandini, M.; Bastiani, M. D.; Pace, G.; Manna, L.; Caironi, M.; Bertarelli, C.; Petrozza, A. *Energy & Environmental Science* **2015**, *8*, 2365.

(39) Deng, Y.; Peng, E.; Shao, Y.; Xiao, Z.; Dong, Q.; Huang, J. *Energy & Environmental Science* **2015**.

(40) Stranks, S. D.; Eperon, G. E.; Grancini, G.; Menelaou, C.; Alcocer, M. J. P.; Leijtens, T.; Herz, L. M.; Petrozza, A.; Snaith, H. J. *Science* **2013**, *342*, 341.

(41) Xing, G.; Mathews, N.; Sun, S.; Lim, S. S.; Lam, Y. M.; Grätzel, M.; Mhaisalkar, S.; Sum, T. C. *Science* **2013**, *342*, 344.

(42) You, J.; Meng, L.; Song, T.-B.; Guo, T.-F.; Yang, Y.; Chang, W.-H.; Hong, Z.; Chen, H.; Zhou, H.; Chen, Q.; Liu, Y.; De Marco, N.; Yang, Y. *Nat Nano* **2015**, *advance online publication*.

(43) Chen, W.; Wu, Y.; Yue, Y.; Liu, J.; Zhang, W.; Yang, X.; Chen, H.; Bi, E.; Ashraful, I.; Grätzel, M.; Han, L. *Science* **2015**, DOI: 10.1126/science.aad1015.